Nanopore-Enabled Dark-Field Digital Sensing (NEDDS) of Nanoparticles

Vignesh Sundaresan^{1*}, Jarek Metro², Allison R Cutri², Milan Palei³, Varun Mannam³, Christiana Oh⁴, Anthony J. Hoffman³, Scott Howard³, and Paul W. Bohn^{2,4*}

¹Department of Chemistry and Biochemistry, University of Mississippi, University, MS 38655 USA

- ² Department of Chemistry and Biochemistry, University of Notre Dame, Notre Dame, IN 46556 USA
- ³ Department of Electrical Engineering, University of Notre Dame, Notre Dame, IN 46556 USA
- ⁴ Department of Chemical and Biomolecular Engineering, University of Notre Dame, Notre Dame, IN 46556 USA

^{*}Authors to whom correspondence should be addressed, vsundare@olemiss.edu, pbohn@nd.edu

Abstract

In this study, we use nanopore arrays as a platform for detecting and characterizing individual nanoparticles (NPs) in real time. Dark-field imaging of nanopores with dimensions smaller than the wavelength of light occurs under conditions where trans-illumination is blocked, while the scattered light propagates to the far-field, making it possible to identify nanopores. The intensity of scattering increases dramatically during insertion of AgNPs into empty nanopores owing to their plasmonic properties. Thus, momentary occupation of a nanopore by a AgNP produces intensity transients that can be analyzed to reveal the following characteristics: 1) NP scattering intensity, which scales with the sixth power of the AgNP radius, shows a normal distribution arising from the heterogeneity in NP size, 2) the nanopore residence time of NPs, which was observed to be stochastic with no permselective effects, and 3) the frequency of AgNP capture events on a 21 × 21 nanopore array, which varies linearly with the concentration of the NPs, agreeing with the frequency calculated from theory. The lower limit of detection (LOD) for NPs was 130 fM, indicating that the measurement can be used in applications where ultrasensitive detection is required. The results presented here provide valuable insights into the dynamics of NP transport into and out of nanopores and highlight the potential of nanopore arrays as a powerful, massively parallel tool for nanoparticle characterization and detection.

Digital sensing of nanoparticles (NPs) and NP-supported biomarkers has recently gained considerable attention due to its capacity to enhance analytical resolution and sensitivity, while also providing nearly background-free signals.^{1,2} Three use cases have attracted significant attention. (1) Optical-based digital sensing methods utilize Au NPs to detect analytes, such as nucleic acids based on particle counting through dark-field microscopy, where probe DNAfunctionalized Au NPs bind to target DNA and are isolated through a sandwich assay with magnetic beads.³ The concentration of the target DNA is determined by counting the released Au NPs, with the number of particles directly corresponding to the target DNA concentration. (2) Walt and co-workers developed the single-molecule optical array (Simoa) approach to detect and quantify biomarkers by utilizing beads to implement immunoassays by encapsulating them individually in microwells.⁴⁻⁷ In this approach, fluorogenic reactions are turned on only if the analyte is present in the bead/microwells, allowing the microwells containing the analyte to be identified. The analyte concentration is obtained by counting the number of strongly emitting microwells using fluorescence microscopy. (3) Finally, electrochemistry-based digital sensing is usually based on counting/quantifying surface collisions or nano-impacts, in which single NPs stochastically collide with an ultramicroelectrode (UME) biased to a well-defined electrochemical potential.^{8–11} The collision generates isolated transient current spikes or steps, which are associated with single NP collision events. This method can be employed to detect both bare NPs and biomarker-functionalized NPs. 12-14 Although these NP-based methods can provide high sensitivity - with LODs in the femtomolar concentration range - their appeal would be enhanced by making them faster and/or non-destructive.

To address the possibility of enhanced digital detection, optical dark-field microscopy is explored

here to monitor the transient capture of single AgNPs in the absence of an electrochemical bias, *i.e.* at open-circuit potential. We employ arrays of nanopores, fabricated to satisfy the requirements of zero-mode waveguide (ZMW) operation, ¹⁵ with pore diameters, d, smaller than a critical value, $d_c \sim \lambda/1.7$, where λ is the excitation wavelength in the medium. Under these conditions, the scattered light intensity from individual nanopores is bimodal, depending on whether or not the specific pore contains either 0 or ≥ 1 AgNP. The ZMW nanopore structure also facilitates the sequestration of single NPs from the bulk and enables the acquisition of reliable scattering intensity-time readouts which narrate the NP occupation history of a given nanopore. Moreover, the array of nanopores enables massively parallel multi-channel data acquisition, resulting in high-throughput analysis. After automating the counting of NP capture events from a 21 × 21 (441) nanopore array an LOD of 130 fM was obtained for 78 nm diameter AgNPs in an acquisition lasting 75 s.

Nanopore arrays were fabricated on a Au-SiO₂ structure as previously reported by our laboratory, and a detailed procedure is provided in the **Supporting Information** (SI).^{16–18} Using this fabrication procedure, an array of 21 x 21 nanopores (a total of 441 nanopores) with an interpore separation of 2 μm was fabricated, as shown in **Figure 1(A)**. The cross-section of an individual nanopore, shown in **Figure S1**, displays an inverted conical frustum with approximate top and bottom diameters of 160 nm and 120 nm, respectively. Next, the entire 21 × 21 nanopore array was imaged using a transmission-based dark-field microscope (DFM, **Figure S2**). DFM image of the nanopore array (**Figure 1(B)**) shows that it blocks the normal transmission of incident light completely, due to the ZMW character of the structure, scattered light from the nanopores is effectively out-coupled and captured in the far-field with the EM-CCD detector. The resulting

image shows an array of bright spots where each bright spot corresponds to an individual nanopore.

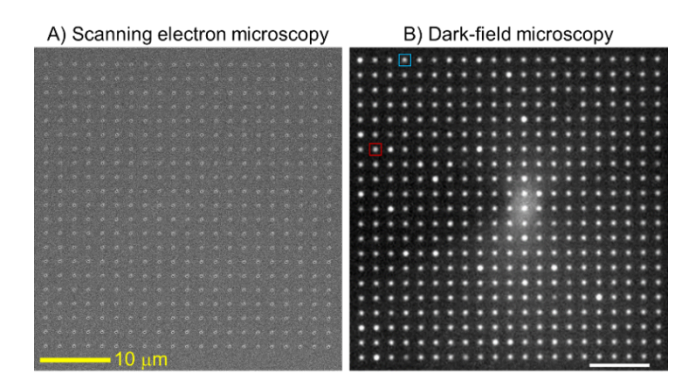


Figure 1. Images of a 21 \times 21 nanopore array. (A) SEM and (B) dark-field microscopy images. Scale bars = 10 μ m.

Next, a solution containing 13 pM $(7.8 \times 10^9 \text{ particles mL}^{-1})$ of 78 nm diameter AgNPs was introduced to the nanopore array substrate and monitored using DFM with individual frame integration times of 50 ms. Under these conditions, the volume-based average occupancy of the individual nanopores with volume 6 aL is $\langle n_{pore} \rangle \sim 4.65 \times 10^{-5}$, and the occupancy for the entire array is $\langle n_{array} \rangle \sim 0.02$. Because the expectation occupancy of any individual nanopore is ~ 0 , the background signal consists of light scattered from nanopores containing only solvent. The introduction of AgNPs caused the nanopore array to exhibit blinking behavior, consisting of transient high-intensity events localized to individual nanopores, which are apparent in **SI video** 1. To analyze the blinking behavior, we used a custom MATLAB code (see **SI Section 4, Figures S3 and S4** for detailed information) to obtain background-subtracted intensities that were plotted as a function of time for each nanopore and used for further analysis.

Figure 2 shows representative intensity-time traces from two different nanopores color coded (red

and blue) in **Figure 1(B)**. At t = 0 s, **Figure 2(A)** shows a low baseline scattering intensity I_{pore} that remains constant until ca. 40 s; this is assigned to empty nanopore scattering. Shortly after 40 s, there is a sharp increase in the intensity, assigned to $I_{pore+NP}$, which then returns back to the I_{pore} after ~ 1 s. Another, somewhat longer, intensity transient is observed at t = 55 - 58 s. Both transients exhibit essentially the same intensity increase over the baseline. We attribute both intensity transients to the stochastic capture and momentary trapping of single NPs within the nanopore. As the AgNP enters the nanopore, the scattering intensity increases due to the localized surface plasmon resonance (LSPR) at the resonant wavelength of the AgNP, as shown schematically in **Figure 2(C)**. The intensity-time trace in **Figure 2(B)** shows another transient response with a much longer residence time ($\tau = 35$ s) of the NP in the nanopore than either of the transients in **Figure 2(A)**. Intensity-time traces of a representative selection of other nanopores are shown in **Figure S5**.

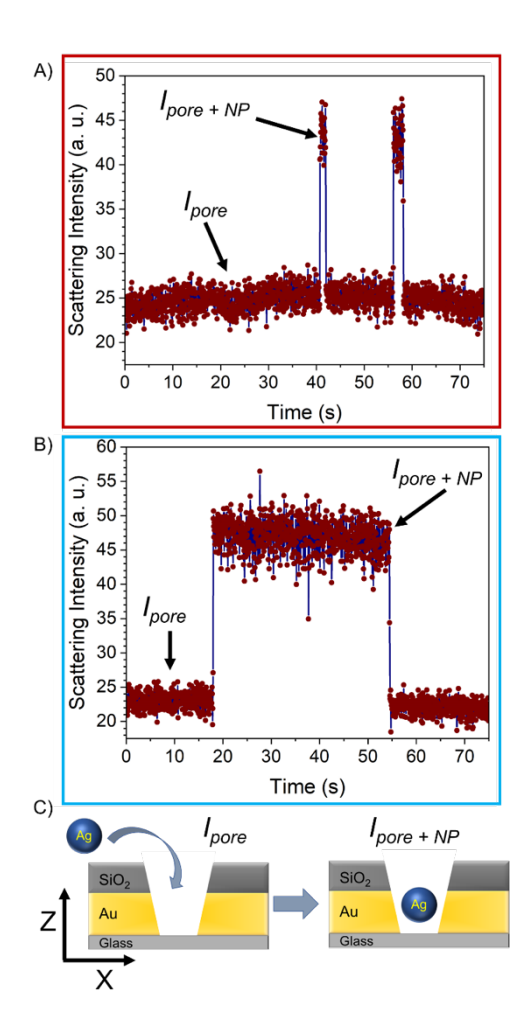


Figure 2. Nanopore scattering behavior in the presence of AgNPs. Intensity-time traces of two nanopores shown in the (A) red and (B) blue boxes in **Figure 1(B)**. (C) Schematic diagram showing a cross-sectional view of a single nanopore before and after the insertion of AgNPs into a nanopore, causing the scattering intensity to increase from I_{pore} to $I_{pore + NP}$.

To better understand the coupling of LSPR modes with nanopore scattering and coupling to the far-field during AgNP insertion, finite-difference time-domain (FDTD) simulations were performed (see **SI Section 6** for details). The electric field distribution for 450 nm radiation propagating through a single unoccupied (*i.e.*, no AgNP) nanopore under dark-field illumination,

shows that the nanopore blocks trans-illumination, and only a small portion (~8 %) of the scattered light is coupled to the far-field, **Figures S6(A)** and **S6(B)**. However, if an 80 nm diameter AgNP is placed at the bottom of the nanopore, a dipolar plasmon mode associated with the AgNP effectively couples to the far field, **Figures S6(C)** and **S6(D)**. In contrast to these results, placing the AgNP at the top or middle of the nanopore structure does not produce dipolar plasmon modes at the bottom of the nanopore, as shown in **Figure S7**. Overall, the FDTD simulation confirms that insertion of AgNPs into the bottom of the nanopore significantly increases the scattering intensity by effectively coupling dipolar plasmon modes to the far-field.

After confirming that the scattering intensity increase is due to transport of AgNPs into the nanopore, the intensity behaviors were analyzed from each of the transients. The intensity increase due to the NP insertion (I_{NP}) was calculated by subtracting I_{pore} from $I_{pore+NP}$ i.e., $I_{NP} = I_{pore+NP} - I_{pore}$. Figure 3(A) shows a histogram of I_{NP} obtained from 1057 intensity-time traces exhibiting a normal distribution with average $\langle I_{NP} \rangle = 17.8$ and standard deviation $\sigma_I = 3.4$. The measured value for I_{NP} depends on two factors: 1) the size of the NP, and 2) the axial (z-axis) position of the NP within the nanopore. The simulations in Figures S6 and S7 show that the NP scattering is strongest when the nanoparticle is located at the bottom of the nanopore, so dispersion in the axial position is less important in determining the I_{NP} distribution in Figure 3(A) than dispersion in the size distribution of the nanoparticles. Assigning the I_{NP} distribution predominantly to heterogeneity in the NP radius also makes sense, because for a plasmonic NP the scattering cross-section is proportional to the sixth power of NP radius as shown in eqn. (1), 19,20

$$\sigma_{scatt} = \frac{8\pi}{3} k^4 R^6 \left| \frac{\epsilon_p - \epsilon_m}{\epsilon_p + 2\epsilon_m} \right| \tag{1}$$

where σ_{scatt} is the scattering cross-section for a spherical NP, k is the wavenumber of the electric field, R is the radius of the NP, and ε_p and ε_m are the relative permittivities of the NP and surrounding medium, respectively.

Further, the distribution of experimentally observed I_{NP} values varies by 19% from the average I_{NP} , which agrees well with the width of the optical scattering cross-section area distribution (~23%) given by Mie theory (See SI Section 7 for details), thus supporting the interpretation that the deviation in the I_{NP} is due to the heterogeneity in the NP size. Additionally, the experiment was repeated employing 62 ± 5 nm diameter AgNPs and the corresponding I_{NP} was analyzed. The histogram of 62 nm AgNPs I_{NP} (Figure S8, blue) shows a smaller average I_{NP} (10.9) in comparison with the I_{NP} of 78 nm diameter AgNPs (17.8) as expected based on eqn. 1.

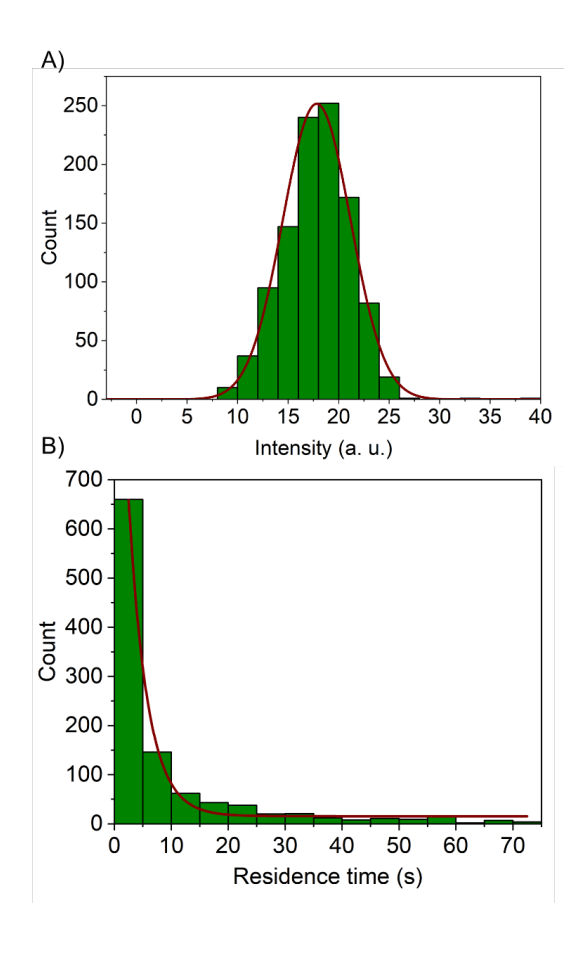


Figure 3. Experimental scattering intensity and residence time distributions for AgNPs in nanopores. A) NP scattering intensity (I_{NP}) histogram with a fit to a normal distribution (red solid line). B) NP residence time (τ) histogram with a fit to an exponential function (red solid line). Both histograms were created by analyzing 1057 intensity-time traces.

Next, the AgNP residence times (τ) within the nanopore were characterized by analyzing the widths of the $I_{pore+NP}$ transients. The histogram of τ values collected from 1057 intensity-time traces is shown in Figure 3(B) exhibits an exponential distribution with a decay constant, τ , of 8.6 s and a median τ of 2.7 s. 62% (655) of the 1057 traces analyzed showed τ less than 5 s, and 76% (802) showed τ less than 10 s. Since the NP is functionalized with citrate, while the nanopore is unfunctionalized, the variation in τ likely arises from a combination of factors - heterogeneity in the NP zeta-potential, surface charge of the nanopore, and the hindered sub-diffusive motion of the NP within the confined nanopore environment. Interestingly, no permselective behavior was observed. The negatively charged SiO₂ nanopore surfaces did not significantly impede the transport of the citrate-capped AgNPs even without additional supporting electrolyte to screen the SiO₂ surface charge, ^{21,22} reflecting relatively small or negligible electrostatic interactions between the NP and the nanopore. Alternatively, when the Au portion of the nanopore was functionalized with biotinylated thiol, and streptavidin-functionalized 60 nm diameter AgNPs were introduced (SI, Section 9), τ values as long ~325 s, Figure S9(A), nearly 40×10^{-2} longer than those observed for citrate-capped AgNPs. The increase in τ reflects the strong affinity between the biotinfunctionalized nanopore and streptavidin-functionalized AgNPs and the effective capture/trapping of the AgNPs.

Next, we calculated the experimental frequency (f_{exp}) of AgNP (concentration = 13 pM) intensity transients on a 21 × 21 array nanopore. In 75 s, 141.8 events were observed on average over three separate experiments, which corresponds to the f_{exp} = 1.89 s⁻¹. The theoretical frequency (f_{th}) of AgNPs entering the recessed nanopore structure was calculated using the following equation,²³

$$f_{th} = \frac{4\pi C_{NP} D_{NP} r^2 N_A N_{pore}}{4L + \pi r} \tag{2}$$

where C_{NP} is the NP concentration, D_{NP} is the NP diffusion coefficient, r is the radius of the nanopore, L is the length of the nanopore, N_A is the Avogadro's number, and N_{pore} is the number of nanopores in the array. It is important to note that eqn. (2) is strictly true for recessed cylindrical structures with uniform radius, and the nanopores used here were conical frustum-shaped with different top and bottom diameters. Nevertheless, the nanopores were approximated as being cylindrical with $r \sim 100$ nm, for which a 13 pM AgNP concentration produces a calculated $f_{th} = 1.56$, which agrees reasonably well with the experimental value $f_{exp} = 1.89 \pm 0.12$. The experiment was then repeated with different concentrations of AgNPs, and the observed total number capture events shows a linear increase with AgNP concentration, as expected, **Figure 4**. The lowest detectable concentration was 0.13 pM which produced 2.3 capture events on average from three 75 s-duration experiments. The values of f_{exp} and f_{the} (**Table S1**) show reasonable agreement for all concentrations 0.13 pM $\leq C \leq 13$ pM.

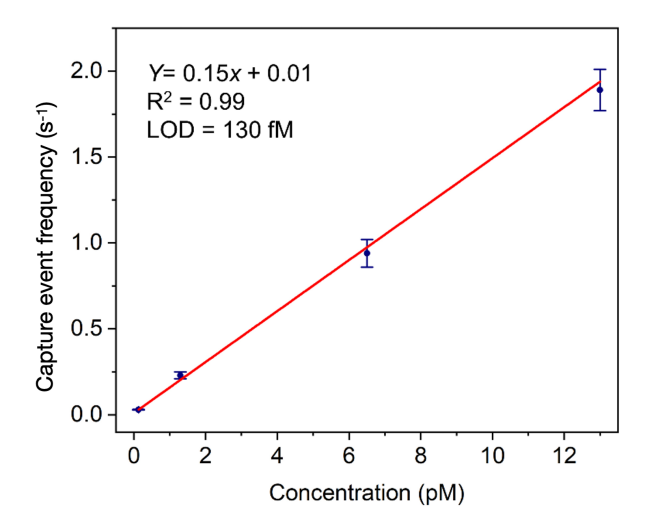


Figure 4. Capture event frequency as a function of AgNP concentration (13, 6.5, 1.3, and 0.13 pM) with a linear fit shown in a red solid line.

In conclusion, optical dark-field scattering has been used to investigate the transient capture of individual AgNPs on a 21 × 21 nanopore array with pore diameters smaller than the wavelength of visible light. The intensity-time traces of individual NP capture events indicate that the scattering intensity increases dramatically upon the insertion of NPs into the nanopore, with scattering being much stronger for NPs near the bottom of the pore, a result confirmed by FDTD simulations. The NP-induced scattering intensities exhibit a normal distribution, which tracks the NP size distribution, and the residence time of citrate-terminated AgNPs in the nanopore is stochastic. Designing the NP surfaces to be chemically complementary to the internal nanopore surfaces produced capture and trapping of individual NPs. Moreover, the frequency of capture events is linear with AgNP concentration, in excellent agreement with the theoretical frequency, with 130 fM being the lowest detectable NP concentration. The nanopore scattering approach developed in this study provides a valuable method for isolating and efficiently examining numerous individual NPs in a highly parallel platform. Furthermore, although not explored here,

the gold optical cladding layer can be used as a working electrode enabling high-throughput correlated optical-electrochemical measurements of single NPs. Lastly, the nanopores can be functionalized with biorecognition elements enabling the detection of biomarker-tagged NPs thus accessing a wide range of diagnostically useful determinations.

Conflicts of interest

There are no conflicts to declare.

Acknowledgments

This work was supported by the National Science Foundation through grant NSF2303574, and by the University of Notre Dame through the Faculty Research Support Program – Initiation Grant. The authors thank the University of Notre Dame Nanofabrication Facility and Notre Dame Integrated Imaging Facility for their assistance with materials fabrication and characterization.

Supporting Information

Supporting Information is available on the Publications website and includes:

- Chemical and materials, fabrication of nanopore array, dark-field imaging experimental setup, the process of analyzing image stacks through MATLAB, additional intensity-time traces with intensity transients, FDTD simulation details, scattering intensity histogram for 78 and 62 nm AgNPs, and residence time analysis for biotin functionalized nanopore and streptavidin labeled AgNPs.
- Video showing the dynamic capture of single nanoparticles in the nanopores. Video recorded at 20 fps and displayed at 200 fps.

Author Information

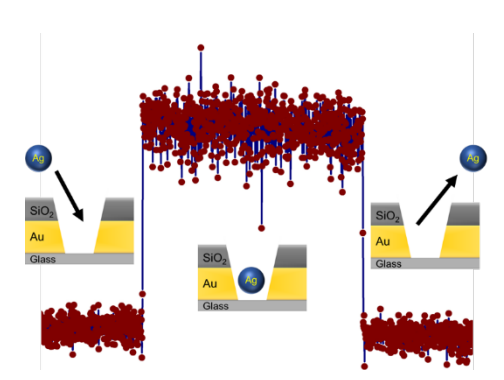
 $Corresponding\ Authors:\ E-mail:\ \textit{vsundare@olemiss.edu}, pbohn@nd.edu$

References

- (1) Krainer, G.; Saar, K. L.; Arter, W. E.; Welsh, T. J.; Czekalska, M. A.; Jacquat, R. P. B.; Peter, Q.; Traberg, W. C.; Pujari, A.; Jayaram, A. K.; Challa, P.; Taylor, C. G.; van der Linden, L.-M.; Franzmann, T.; Owens, R. M.; Alberti, S.; Klenerman, D.; Knowles, T. P. J. *Nat. Commun.* **2023**, *14* (1), 653.
- (2) Cretich, M.; Daaboul, G. G.; Sola, L.; Ünlü, M. S.; Chiari, M. *Trends Biotechnol.* **2015**, *33* (6), 343–351.
- (3) Li, T.; Xu, X.; Zhang, G.; Lin, R.; Chen, Y.; Li, C.; Liu, F.; Li, N. Anal. Chem. **2016**, 88 (8), 4188–4191.
- (4) Rissin, D. M.; Kan, C. W.; Campbell, T. G.; Howes, S. C.; Fournier, D. R.; Song, L.; Piech, T.; Patel, P. P.; Chang, L.; Rivnak, A. J.; Ferrell, E. P.; Randall, J. D.; Provuncher, G. K.; Walt, D. R.; Duffy, D. C. *Nat. Biotechnol.* 2010, 28 (6), 595–599.
- (5) Wu, C.; Maley, A. M.; Walt, D. R. Crit. Rev. Clin. Lab. Sci. 2020, 57 (4), 270–290.
- (6) Gilboa, T.; Cohen, L.; Cheng, C.-A.; Lazarovits, R.; Uwamanzu-Nna, A.; Han, I.; Griswold Jr., K.; Barry, N.; Thompson, D. B.; Kohman, R. E.; Woolley, A. E.; Karlson, E. W.; Walt, D. R. Angew. Chem. Int. Ed. 2021, 60 (49), 25966–25972.
- (7) Wu, C.; Dougan, T. J.; Walt, D. R. ACS Nano 2022, 16 (1), 1025–1035.
- (8) Xu, W.; Zou, G.; Hou, H.; Ji, X. Small 2019, 15 (32), 1804908. https://doi.org/10.1002/smll.201804908.
- (9) Defnet, P. A.; Anderson, T. J.; Zhang, B. Curr. Opin. Electrochem. 2020, 22, 129–135.
- (10) Stevenson, K. J.; Tschulik, K. A. Curr. Opin. Electrochem. 2017, 6 (1), 38–45.
- (11) Glasscott, M. W.; Dick, J. E. Anal. Chem. **2018**, 90 (13), 7804–7808.
- (12) Sekretareva, A. Sensors and Actuators Reports 2021, 3, 100037.

- (13) Qiu, X.; Tang, H.; Dong, J.; Wang, C.; Li, Y. Anal. Chem. 2022, 94 (23), 8202–8208.
- (14) Dick, J. E.; Hilterbrand, A. T.; Strawsine, L. M.; Upton, J. W.; Bard, A. J. Proc. Natl. Acad. Sci. 2016, 113 (23), 6403–6408..
- (15) Levene, M. J.; Korlach, J.; Turner, S. W.; Foquet, M.; Craighead, H. G.; Webb, W. W.. *Science* **2003**, *299* (5607), 682–686.
- (16) Sundaresan, V.; Bohn, P. W. Chem. Sci. 2020, 11 (40), 10951–10958.
- (17) Baek, S.; Han, D.; Kwon, S.-R.; Sundaresan, V.; Bohn, P. W. *Anal. Chem.* **2022**, *94* (9), 3970–3977.
- (18) Baek, S.; Cutri, A. R.; Han, D.; Kwon, S.-R.; Reitemeier, J.; Sundaresan, V.; Bohn, P. W. J. Appl. Phys. 2022, 132 (17), 174501.
- (19) Dijk, M. A. van; Tchebotareva, A. L.; Orrit, M.; Lippitz, M.; Berciaud, S.; Lasne, D.; Cognet, L.; Lounis, B. *Phys. Chem. Chem. Phys.* **2006**, *8* (30), 3486–3495.
- (20) Tcherniak, A.; Ha, J. W.; Dominguez-Medina, S.; Slaughter, L. S.; Link, S. *Nano Lett.* **2010**, 10 (4), 1398–1404.
- (21) Fu, K.; Bohn, P. W. ACS Cent. Sci. 2018, 4 (1), 20–29.
- (22) Fu, K.; Han, D.; Crouch, G. M.; Kwon, S.-R.; Bohn, P. W. Small 2018, 14 (18), 1703248.
- (23) Arrigan, D. W. M. Analyst 2004, 129 (12), 1157–1165.

For TOC only



Supporting Information for

Nanopore-Enabled Dark-Field Digital Sensing (NEDDS) of Nanoparticles

Vignesh Sundaresan^{1*}, Jarek Metro², Allison R Cutri², Milan Palei³, Varun Mannam³, Christiana Oh⁴, Anthony J. Hoffman³, Scott Howard³, and Paul W. Bohn^{2,4*}

¹Department of Chemistry and Biochemistry, University of Mississippi, University, MS 38655 USA

² Department of Chemistry and Biochemistry, University of Notre Dame, Notre Dame, IN 46556 USA

³ Department of Electrical Engineering, University of Notre Dame, Notre Dame, IN 46556 USA

⁴ Department of Chemical and Biomolecular Engineering, University of Notre Dame, Notre Dame, IN 46556 USA

Table of Contents

1.	Chemicals and Materials	3
2.	Fabrication of Nanopore Arrays	3
3.	Optical Dark-Field Imaging	4
4.	Image Stack Analysis Workflow	5
5.	Representative Intensity-Time Traces	8
6.	FDTD Simulations	9
7.	Nanoparticle scattering cross-sectional area	13
8.	Scattering Intensities for 78 and 62 nm Ag NPs	14
9.	Residence Time Analysis for Functionalized Nanopore-NP Pairs.	15
10.	Table S1: Experimental and Theoretical Capture Frequencies for 78 nm Ag NPs	16
Ref	erences:	16

1. Chemicals and Materials

Citrate-capped 78 ± 9 and 62 ± 5 nm diameter Ag NPs (NanoXact Silver Nanospheres) were purchased from Nanocomposix. 60 nm diameter streptavidin labeled Ag NPs (SNP60-SV-1) and Thiol PEG Biotin (PG2BNTH-400) were purchased from NANOCS. Sodium citrate tribasic dihydrate (#71402) was purchased from Sigma Aldrich. Glass coverslips (Nexterion Uncoated High-Performance 1.5H Coverslips, Glass D263) were purchased from Applied Microarrays. All aqueous solutions were prepared with deionized (DI) water (18 M Ω -cm, Millipore Milli-Q water purification system). All materials were used as received without further purification.

2. Fabrication of Nanopore Arrays

The procedure for the nanopore array fabrication was reported in our previous publication.¹ Initially, a 10 nm titanium adhesion layer was deposited on a clean glass coverslip via electron-beam evaporation, followed by a 200 nm gold film using a custom-made shadow mask. Subsequently, a 100 nm SiO₂ layer was deposited on the gold film via plasma-enhanced chemical vapor deposition. Finally, a dual-source SEM-FIB instrument was utilized to mill and analyze the nanopore arrays, with FIB parameters set at 30 kV acceleration, 0.26 nA ion current, 100 µs dwell time, 2 µm pitch, and 2 nm Z-depth. The fabricated arrays were thoroughly rinsed with DI water and then utilized for dark-field imaging experiments. The top and the cross-sectional view of a single nanopore in the array are shown in **Figure S1**.

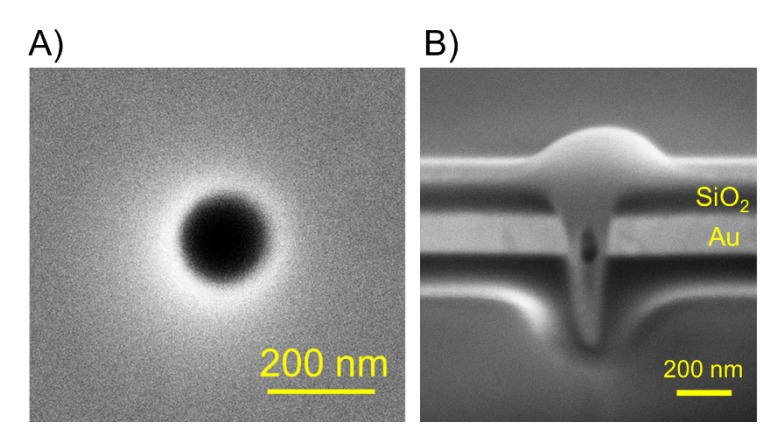


Figure S1. A) Magnified plan view SEM image of one nanopore. B) Cross-sectional SEM view of single pore showing 200 nm thick Au and 10 nm thick SiO₂ hierarchical layers.

3. Optical Dark-Field Imaging

Nanopore arrays were placed on an inverted optical microscope (Olympus-IX 71) equipped with a 100× objective (Olympus oil immersion, NA 0.6). White light from a tungsten-halogen source was directed through the dark-field condenser to illuminate the nanopore arrays from the SiO₂ side, and the scattered low-angle light from the nanopore and/or Ag NPs was collected and imaged onto an electron multiplier-CCD camera (Princeton Instruments). The experimental apparatus is depicted schematically in **Figure S2**. Each experiment involved capturing 1500 images with an integration time of 50 ms/frame, for a total acquisition time of 75 s. The image stacks or movies obtained were saved as .tiff files and subsequently analyzed using MATLAB and ImageJ.

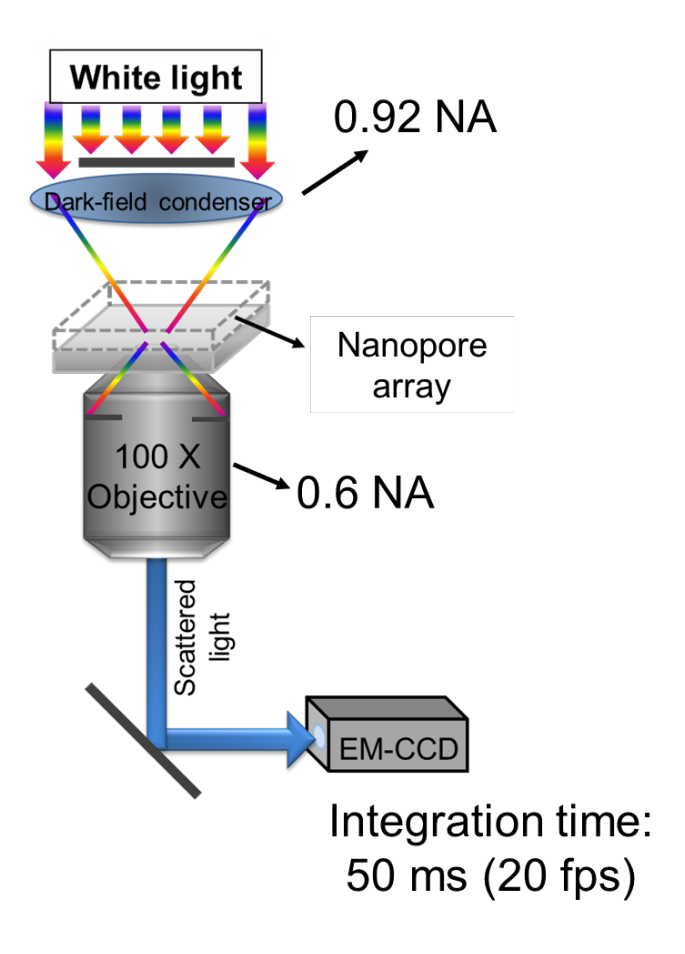


Figure S2. Schematic diagram of the dark-field microscopy instrument.

4. Image Stack Analysis Workflow

The process used to analyze the image stacks in MATLAB is shown in **Figure S3**. Initially, each movie consisting of 1500 image stacks was imported into MATLAB, **Figure S3(A)**. Subsequently, ImageSegmenter was utilized with an adaptive threshold and sensitivity of 0 to selectively highlight the nanopores, as shown in **Figure S3(B)**. The image was then binarized, with nanopores being assigned a pixel value of 1, while the non-pore area was assigned a pixel value of 0, **Figure S3(C)**. The center position of each nanopore was then determined using the binarized image and recorded separately. Thereafter, a 7×7 pixel region (three pixels from the center pixel on all four sides) around the nanopore was designated as a region of interest (ROI), and the intensities in each

ROI, **Figure S3(D)** yellow box, were integrated. Additionally, a separate 7×7 pixel background ROI was identified in an area just adjacent to the nanopore ROI, **Figure S3(D)** red box. The intensities within the background ROI were integrated and the resulting background was subtracted from the nanopore ROI for each detected nanopore. The resulting array of background-subtracted intensity values was then used for all subsequent analysis.

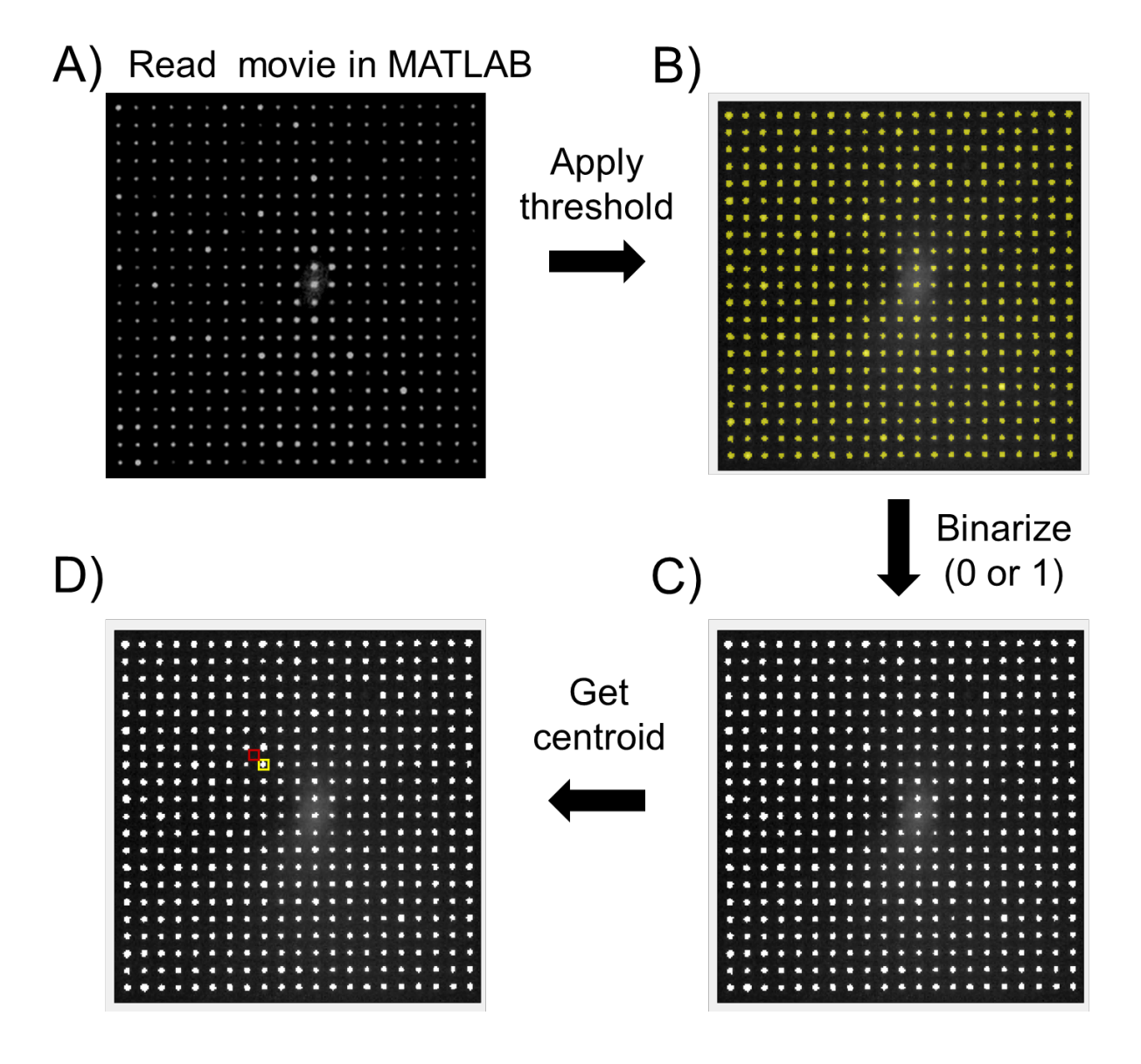


Figure S3. Step-by-step workflow for image stack analysis using MATLAB. A) Raw dark-field image stacks ready for analysis. B) Nanopore regions identified using MATLAB ImageSegmenter

are shown in yellow. C) Binarize the image, white represents value of 1 and black represents value of the 0. D) Determine the center of each nanopore ROI detected and use this position to define a 7×7 pixel ROI around the nanopore (yellow box) and a nearby background 7×7 pixel ROI (red box).

For each movie analyzed, the output files contain: (1) one text file containing all the background subtracted intensity-time traces for all the detected nanopores; (2) a composite nanopore array image with a pore index as shown in **Figure S4**; and (3) intensity-time plots for each nanopore with a file name "Pore-x", where x is the pore index as given in **Figure S4**.

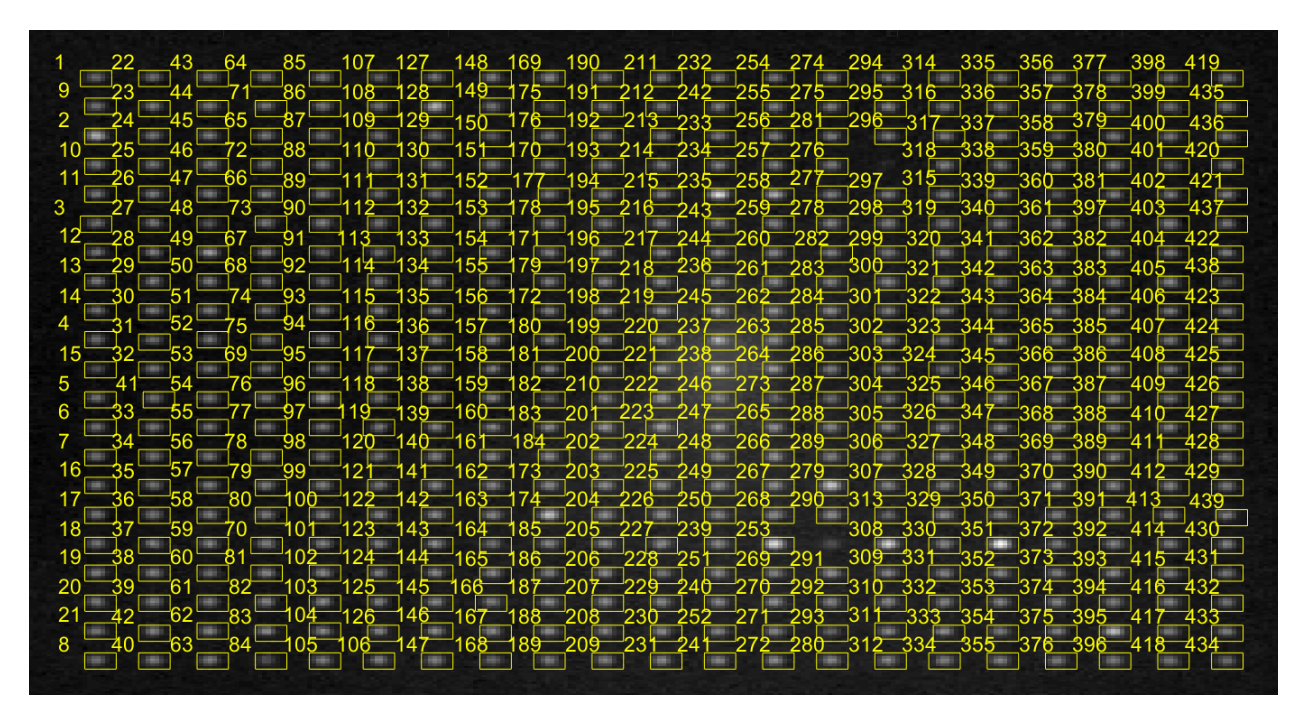


Figure S4. Composite image of the dark-field image stacks with the detected pores (yellow boxes) and their corresponding pore index (yellow numbers).

Lastly, the peak intensities and residence timees were calculated by analyzing the text file containing all the background subtracted intensity-time traces using another custom MATLAB

code. For each intensity trace corresponding to a nanopore, the code identified the number of points with intensities exceeding 3σ from the average baseline, averaged them to obtain $I_{pore + NP}$, and subtracted the baseline average, I_{pore} , from them to obtain I_{NP} . Multiplying the number of points by the integration time of the EM-CCD yielded the residence time, τ .

5. Representative Intensity-Time Traces

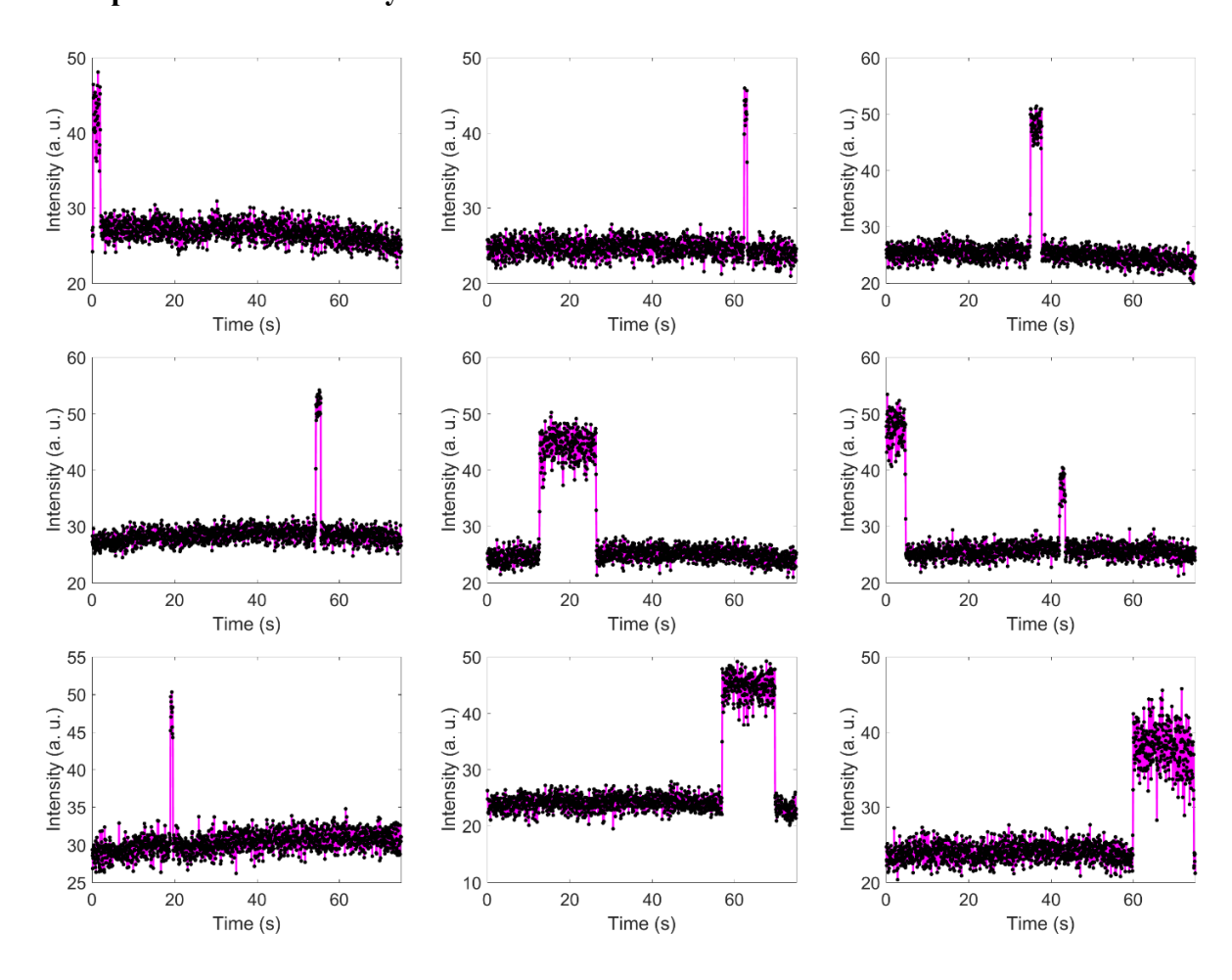


Figure S5. Intensity-time traces of nine different nanopores with 13 pM of 78 nm diameter Ag NPs exhibiting a range of intensity transient behaviors.

6. FDTD Simulations

Numerical Simulation: Scattering of silver nanoparticle in nanopores was simulated using Lumerical FDTD software from ANSYS. The structural parameters of silver nanoparticles and of the nanopore were obtained from SEM and incorporated into the simulation. The complex dielectric function of SiO₂, gold and silver were obtained from Johnson-Christy and Palik, respectively.^{2,3} In the dark-field scattering simulations, the dark-field source is constructed by two Gaussian beams consisting of two concentric rings with slightly different amplitudes and a phase difference of π .⁴ This results in a destructive field in the overlapping region of two Gaussian beams. A confocal dark-field light source is generated by tuning the virtual NAs of the inner and outer Gaussian beams. Both in-plane '*x-y*' and out-of-plane or cross-section '*x-z*' electric field profiles are recorded by placing a frequency domain field and power monitor in the center of the nanoparticles and output end of the nanopore. A mesh resolution of 10 nm was used in all simulations.

Figure S6(A) shows a cross-sectional view (x-z plane) of the electric field distribution for 450 nm radiation propagating through a single unoccupied (i.e., no AgNP) nanopore under dark-field illumination, and **Figure S6(B)** shows the electric field distribution in the x-y plane for the same nanopore at the bottom of the Au layer, i.e., at a depth indicated by the yellow dashed line in **Figure S6(A)**. As expected, the nanopore blocks trans-illumination, and only a small portion of the scattered light is coupled to the far-field as evidenced by \sim 92 % drop in the intensity maximum from entry to the transmission/scattering point, cf. **Figures S6(A)** and **S6(B)**. However, if an 80 nm diameter AgNP is placed at the bottom of the nanopore, **Figure S6(C)**, the x-y plane displays a dipolar plasmon mode associated with the AgNP which effectively couples to the far field, as

evidenced by the intensity distributions in **Figure S6(D)**. It is important to note that the simulation was performed at $\lambda = 450$ nm, to match the LSPR of 80 nm diameter AgNPs ($\lambda_{peak} = 463$ nm). In contrast to these results, placing the AgNP at the top or middle of the nanopore structure does not produce dipolar plasmon modes at the bottom of the nanopore, as shown in **Figure S7**. Overall, the FDTD simulations confirm that insertion of AgNPs into the nanopore significantly increases the scattering intensity by effectively coupling dipolar plasmon modes to the far-field. In addition, the scattered intensity is strongest when the NP is at the bottom of the nanopore.

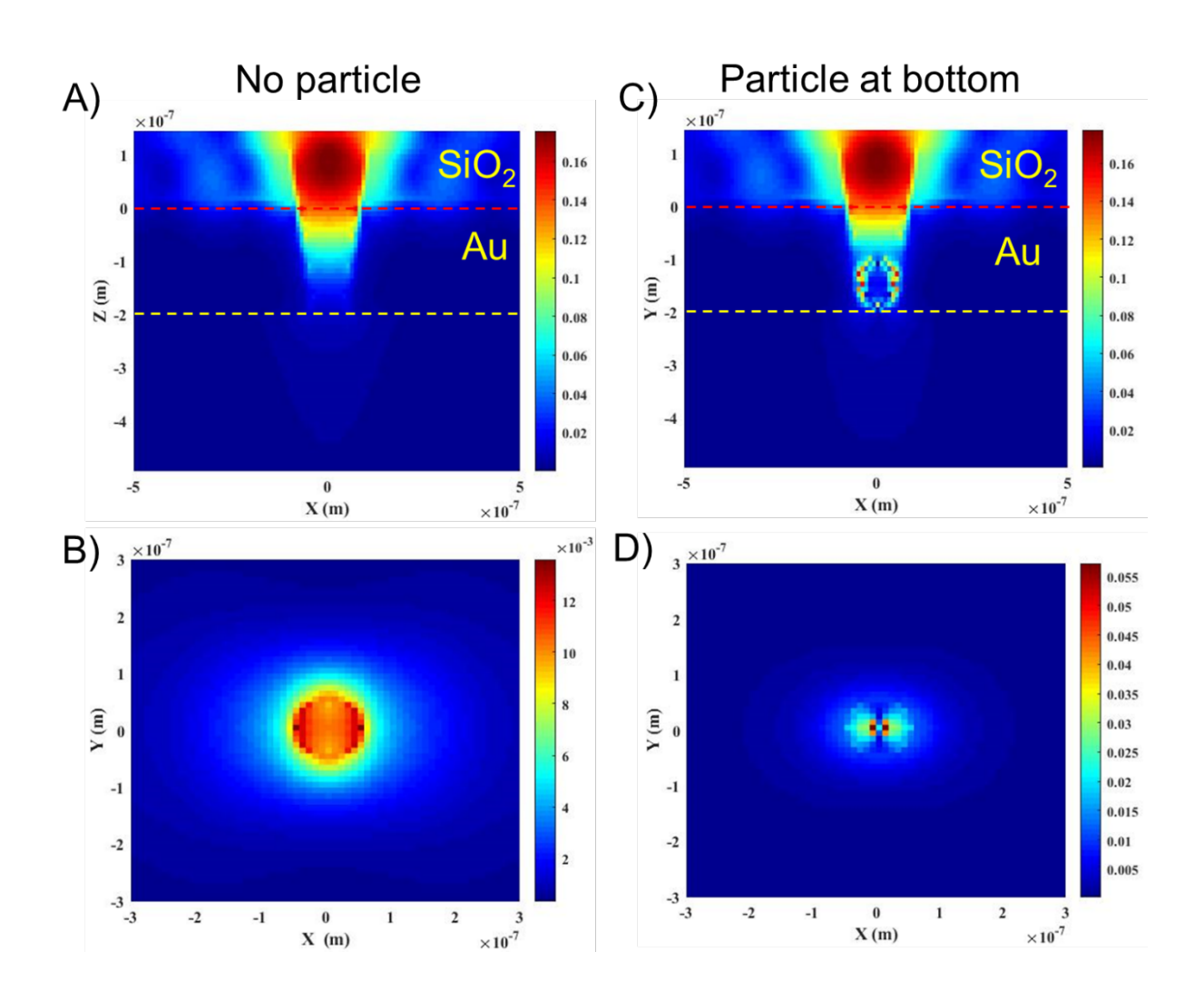


Figure S6. Electric field spatial distributions for nanopore/NP systems. (A) and (B) FDTD simulations of electric field distributions in the x-z (A) and x-y (B) planes for an unoccupied nanopore. (C) and (D) FDTD simulations of electric field distributions in the x-z (C) and x-y (D) planes for a nanopore with an 80 nm AgNPs under dark-field illumination. (A) and (C) show a cross-sectional view (x-z) of the nanopore, while (B) and (D) show the x-y plane of the nanopore at the depth r indicated by the yellow dashed lines in (A) and (C), respectively, i.e., at the bottom of the gold layer.

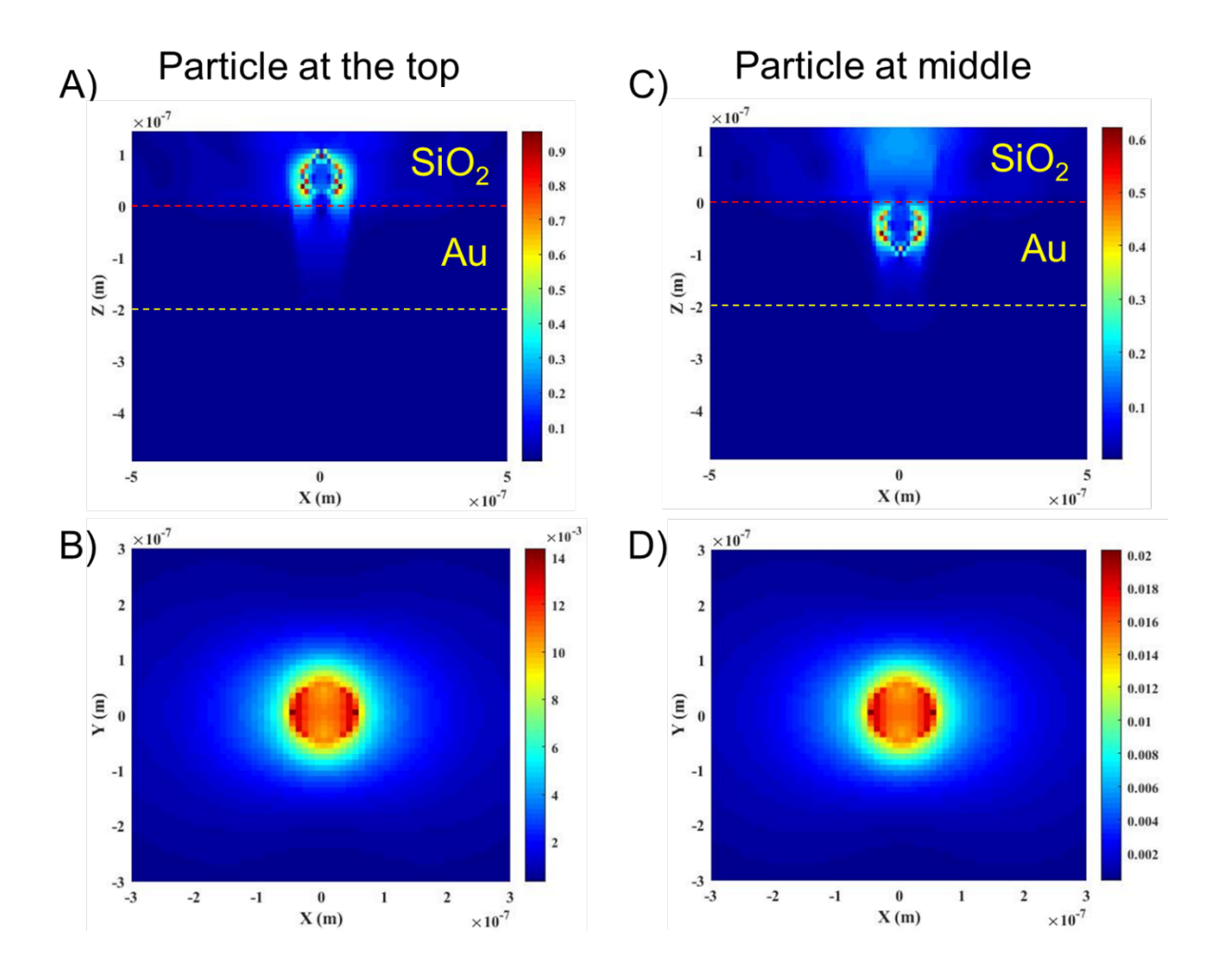


Figure S7. Electric field distributions. FDTD simulation of electric field distribution for nanopore with the 80 nm Ag NPs at the top (A) and (B) and middle (C) and (D) of the nanopore under dark-field illumination. (A) and (C) show cross-sectional (x-z) views of the nanopore. (B) and (D) show intensities along the x-y plane of the nanopore at the bottom of the gold layer indicated by the yellow dashed lines in (A) and (C), respectively.

7. Nanoparticle scattering cross-sectional area

The scattering cross-section was calculated using nanoComposix Mie theory calculator⁵ based on the nanoparticle particle diameter distribution, 78 ± 9 nm. The peak scattering cross-sectional area of 78 nm diameter AgNPs is 3.44×10^4 nm², whereas, the scattering cross-sectional area of 69, and 87 nm diameter AgNPs are 2.62×10^4 nm², and 4.20×10^4 nm², respectively, giving a deviation of ~23% from the average NP diameter (78 nm) scattering cross-section.

8. Scattering Intensities for 78 and 62 nm Ag NPs

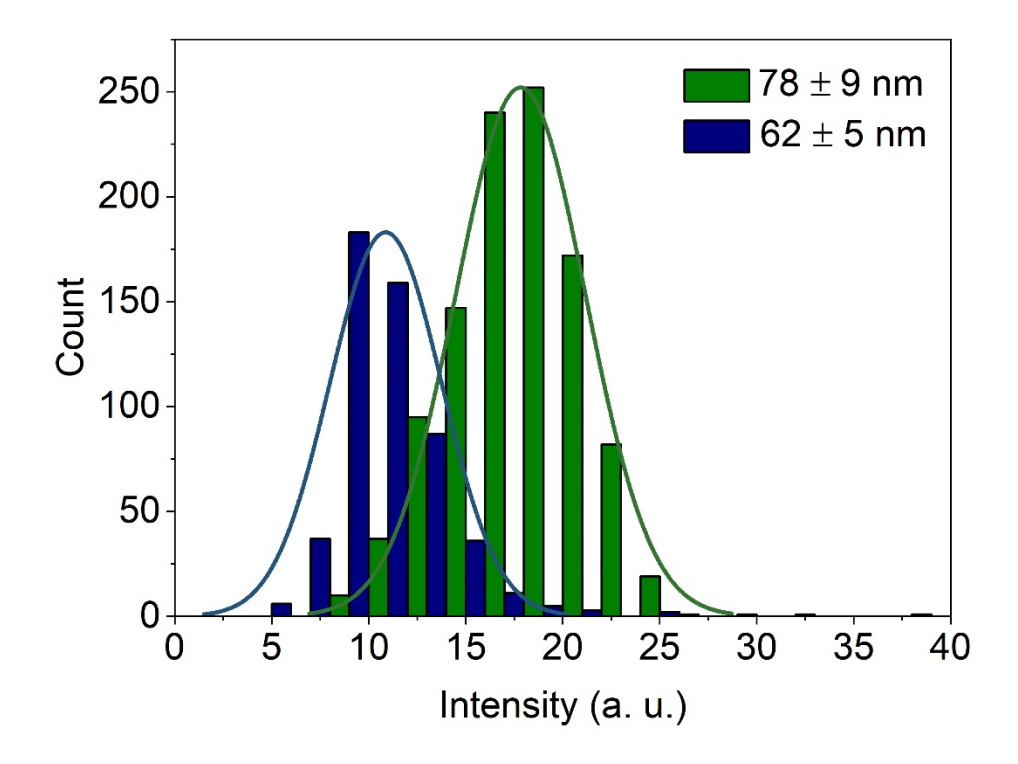


Figure S8. NP scattering intensity (I_{NP}) histogram with a fit to a normal distribution (solid lines) for two different AgNP sizes, blue -62 nm (from 530 intensity-time traces), and green -78 nm (from 1057 intensity-time traces) diameter AgNPs.

9. Residence Time Analysis for Functionalized Nanopore-NP Pairs.

To explore NP-nanopore interactions, the Au portion of the nanopore was functionalized with biotinylated thiol, and streptavidin-functionalized 60 nm diameter AgNPs were introduced. We hypothesized that the high biotin-streptavidin binding affinity would result in NPs entering the nanopore being captured/trapped inside the nanopore, thus shifting the distribution of τ values to longer times. Nanopores with biotin in the presence of AgNPs with streptavidin exhibit τ values as long ~325 s, see **Figure S9(A)**, nearly 40× longer than those observed for citrate-capped AgNPs. Additionally, out of 1021 intensity time traces analyzed, ~92% showed $\tau \ge 75$ s (acquisition time for one movie) as shown in the τ histograms in **Figure S9(B)**.

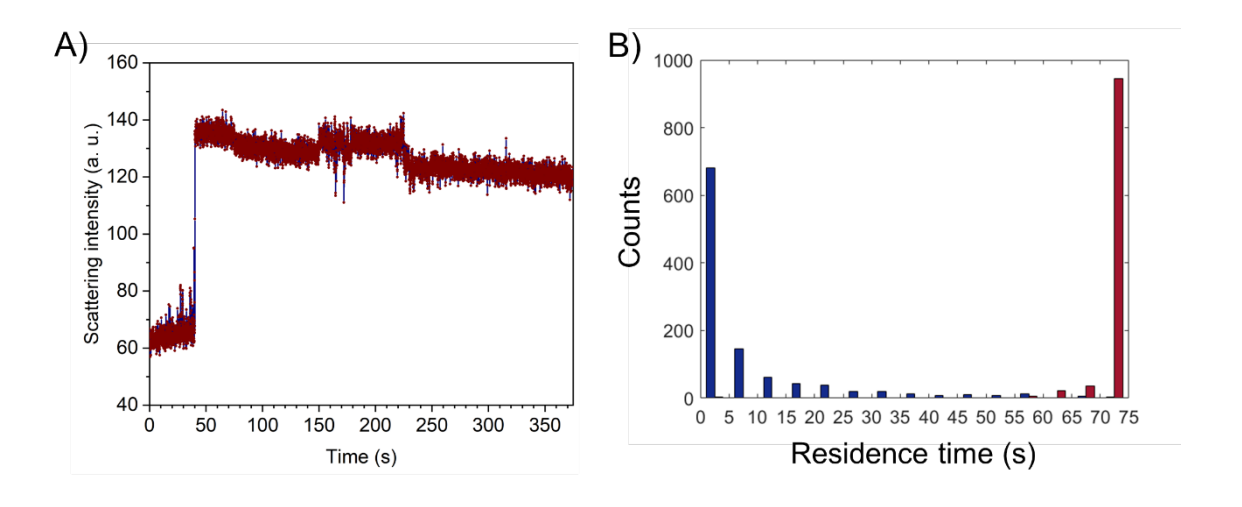


Figure S9. Residence time analysis for functionalized nanopore-NP pairs. (A) Representative intensity-time trace for the insertion of streptavidin labeled 60 nm Ag NPs in biotin functionalized nanopores obtained by merging 5 individual intensity time traces, each of 75 s. (B) NP residence time (τ) histogram for the 80 nm citrate-terminated Ag NPs with unfunctionalized nanopore (blue) and 60 nm streptavidin-labeled AgNPs with biotin functionalized nanopore (red).

10. Table S1: Experimental and Theoretical Capture Frequencies for 78 nm Ag NPs

Concentration of Ag	Experimental	Theoretical frequency,	Difference
NPs (pM)	frequency, f_{exp} (s ⁻¹) for	f_{the} (s ⁻¹) for 441	$(f_{exp}-f_{the})\%$
	441 nanopores	nanopores	
13	1.89	1.56	17.5
6.5	0.94	0.78	17.02
1.3	0.23	0.16	30.43
0.13	0.03	0.016	46.6

References:

- 1) V. Sundaresan, and P. W. Bohn, "Acid-Base Chemistry at the Single Ion Limit", Chem. Sci., **2020**, *11*, 10951-10958
- 2) P. B. Johnson, and R. W. Christy, "Optical Constants of the Noble Metals", Phys. Rev. B, **1972**, *6*, 4370
- 3) H. R. Philipp, "Silicon dioxide (SiO₂) glass," in Handbook of Optical Constants of Solids, E. D. Palik, ed. (Academic, 1985), Vol. I, pp. 749. (SiO₂)
- 4) L. Jiang, T. Yin, Z. Dong, M. Liao S. J. Tan, X. M. Goh, D. Alliou, H. Hu, X. Li, J. K. W. Yang, and Z. Shen, "Accurate Modeling of Dark-Field Scattering Spectra of Plasmonic Nanostructures", ACS Nano **2015**, *9*, 10039–10046
- 5) nanoComposix. *Mie Theory Calculator*. nanoComposix. https://nanocomposix.com/pages/mie-theory-calculator